OATAO

Open Archive Toulouse Archive Ouverte

Open Archive Toulouse Archive Ouverte (OATAO)

OATAO is an open access repository that collects the work of some Toulouse researchers and makes it freely available over the web where possible.

This is an author's version published in: https://oatao.univ-toulouse.fr/26532

Official URL:

To cite this version :

Correlation-Based Radar Receivers with Pulse-Shaped OFDM Signals

Steven Mercier*, Damien Roque*, Stéphanie Bidon* and Cyrille Enderli†

*ISAE-SUPAERO, Université de Toulouse, France

Email: {steven.mercier,stephanie.bidon,damien.roque}@isae-supaero.fr

†Thales DMS, Élancourt, France

Email: cyrille-jean.enderli@fr.thalesgroup.com

Abstract—In waveform sharing scenarios, various radar receivers have been developed for orthogonal frequency-division multiplexing (OFDM) signals. More general waveforms, such as pulse-shaped multicarrier modulations received little attention so far, despite their increased robustness to high-Doppler scatterers.

In this paper, we compare the performance of two correlation-based radar receivers, namely the matched filter and the symbol-based technique, when used with different pulse-shaped multicarrier waveforms. We express the signal-to-interference-plus-noise-ratio in the range-Doppler map, taking into account the pedestal (or random sidelobes) induced by the symbols. Benefits of pulse shaping is further illustrated in a realistic vehicular scenario, in presence of multiple targets and ground clutter. In this context, the symbol-based approach outperforms the matched filter while enjoying a low-computational complexity.

More generally, our results reveal the multicarrier pulse shape as a relevant degree of freedom in waveform co-design approaches (*e.g.*, cognitive radar/communication systems).

I. INTRODUCTION

Dual-functional radar-communication (DFRC) systems are intended to decongest the radio spectrum while sharing a single hardware platform [1]. They rely on a joint waveform design to simultaneously perform both functionalities (Fig. 1). In various applications such as vehicular networks, multicarrier modulations are usually good candidates to accommodate highly time-frequency selective radar and communication channels [2].

From a correlation-based radar receiver viewpoint, the symbols carried by the multicarrier waveform can be seen as a nuisance parameter, inducing a pedestal (or random sidelobes) in the range-Doppler map. While such an interference has been studied in the particular case of cyclic-prefix orthogonal frequency-division multiplexing (CP-OFDM) [3], a generalization to pulse-shaped multicarrier schemes (*e.g.*, FBMC[1], FMT[2] [4]) is of interest to increase the robustness of DFRC systems towards high-Doppler and/or low signal-to-noise-ratio scenarios [5], [6].

In this paper, we quantify the impact of that limitation in the context of weighted cyclic prefix (WCP)-OFDM waveforms [7], which are an extension of the conventional CP-OFDM to possibly non-rectangular pulse-shapes while pre-

[1]Filter Bank based MultiCarrier.
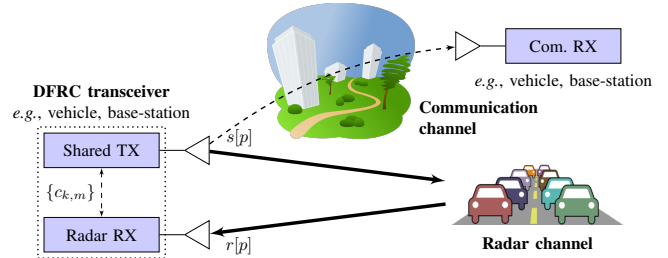
[2]Filtered MultiTone.

Fig. 1. Vehicular DFRC scenario involving a shared waveform to simultaneously perform radar sensing and data transmission. The radar transceiver is monostatic with a perfect knowledge of the symbol sequence.

serving a low-complexity implementation. Two remarkable correlation-based radar receivers are especially considered: the well-known matched filter (MF), and the so-called symbol-based (SB) processing [8]. We first compare their signal-to-interference-plus-noise-ratio (SINR) in response to a single-scatterer scenario, for both time-frequency localized (TFL) and rectangular pulse-shaped transmissions (the latter being the CP-OFDM baseline). The benefits of pulse-shaping is then further exemplified in a simulated realistic monostatic vehicular scenario, including several targets and ground clutter.

Notation: $\mathcal{I}_N$ denotes the finite set $\{0, \dots, N-1\}$ and $\backslash$ the set difference. $\mathbb{E}\{\cdot\}$ is the expectation operator, $\|\cdot\|$ the ℓ_2-norm and sgn is the *signum* function anywhere but in 0 where we set $\mathrm{sgn}(0) \triangleq 1$.

II. MULTICARRIER RADAR SYSTEM

In this Section, we describe the radar "path" depicted in Fig. 1 (thick arrows). A detailed performance study of the communication link falls beyond the scope of this paper.

A. Shared multicarrier transmitter

The DFRC transmitter generates M blocks (or sweeps) of K orthogonal subcarriers over an instantaneous bandwidth B around a carrier frequency F_c. Each block/subcarrier carries a complex data symbol $c_{k,m}$ with $(k,m) \in \mathcal{I}_K \times \mathcal{I}_M$. Assuming $K \gg 1$, the critically sampled transmitted signal is [9]

$$s[p] \triangleq \sum_{m=0}^{M-1} \left(\frac{1}{\sqrt{K}} \sum_{k=0}^{K-1} c_{k,m} e^{j2\pi \frac{k}{K}(p-mL)} \right) g[p-mL] \quad (1)$$

where g is the *transmit* pulse-shape and $L \geq K$ is the discrete-time pulse repetition interval. In the following, symbols are assumed independent and uniformly distributed, drawn from a zero-mean unit-variance constellation of size N. The raw spectral efficiency of the system is thus $\eta = \log_2(N)K/L$. To ensure a low-complexity implementation of (1) in the time-domain, we focus on short pulses (*i.e.*, $g[p] = 0$ for $p \notin \mathcal{I}_L$ [7]).

B. Radar channel

Target: While it propagates towards the communication receiver at light speed c, part of the narrowband signal (1) is backscattered to the DFRC transceiver by a target. The latter is described as a single point object with: a zero-mean complex amplitude α; a radial velocity v and an attendant Doppler frequency $F_d \triangleq 2vF_c/c$; an unambiguous range $R_0 = l_0\delta_R$ with $l_0 \in \mathcal{I}_K$ the range gate and $\delta_R \triangleq c/(2B)$ the radar range resolution. Provided that $F_d \ll B$, the baseband target signal at the input of the radar receiver is sampled at rate B to yield [9]

$$r_t[p] = \alpha \exp(j2\pi F_d p/B)s[p - l_0]. \tag{2}$$

Ground clutter: Presence of ground echoes in the received radar signal may also be expected. We model ground clutter as a contiguous set of statistically independent patches in range and azimuth. Especially, at each range bin $i_c \in \mathcal{J}_c$ with $\mathcal{J}_c \triangleq \mathcal{I}_K \setminus \mathcal{I}_{\lfloor h_r/\delta_R \rfloor}$ where h_r denotes the system altitude and $\lfloor \cdot \rfloor$ the floor function, we assume N_c equally spaced patches around the radar. As for the target, each patch is characterized by: a zero-mean complex amplitude ρ_{i_c,n_c}; a nominal Doppler frequency $F_{d_{i_c,n_c}} \ll B$. Consequently, the received baseband clutter signal sampled at rate B is given by

$$r_c[p] = \sum_{i_c \in \mathcal{J}_c} \sum_{n_c \in \mathcal{I}_{N_c}} \rho_{i_c,n_c} \exp(j2\pi F_{d_{i_c,n_c}} p/B)s[p - i_c]. \tag{3}$$

Apart from the realistic scenario under consideration in Section IV, we will presume in the following that $r_c[p] = 0$.

Additive thermal noise: A thermal noise contribution w, modeled as a zero-mean white circular Gaussian process with variance σ^2, finally adds up to (2) and (3), yielding the full received baseband radar signal

$$r[p] = \begin{cases} r_t[p] + r_c[p] + w[p] & \text{if } p \in \mathcal{I}_{LM}, \\ 0 & \text{otherwise.} \end{cases} \tag{4}$$

Truncation to LM samples in (4) enables a coherent processing interval (CPI) restricted to the transmitted signal length, thus preserving compact notation in the upcoming derivations. In most realistic scenarios (*e.g.*, $M \gg 1$) a negligible integration loss is reported.

C. Correlation-based radar receivers

With the aim of detecting and estimating the target, (4) is usually represented in the range-Doppler domain[3]. Among the

---

[3]In numerous scenarios, such transformation is preceded by a clutter mitigation stage (*e.g.*, whitening). The latter is however out of the scope of this work.

---

variety of correlation-based receivers that have accordingly been proposed, two stand out [3]. These are recalled hereafter with a normalization factor chosen to ensure the same processing gain for a target at null range and Doppler.

Matched filter (MF): The matched filter is a classical radar receiver that consists in cross-correlating the received signal (4) with Doppler shifted versions of the transmitted signal (1). It can be written

$$\chi_{\text{MF}}[l,n] \triangleq \frac{1}{\sqrt{KM}} \sum_{p=0}^{LM-1} r[p]s^*[p - l]e^{-j2\pi\frac{n}{ML}p}. \tag{5}$$

While it is known to be the optimum linear filter in terms of signal-to-noise-ratio (SNR) in presence of white noise, such a performance criterion is not necessarily adequate for information-bearing signals, as discussed hereafter in Subsection II-D.

Symbol-based (SB): The so-called symbol-based radar receiver can be seen as a simplification of the MF relying on (i) an invariant Doppler approximation for each block, (ii) the exploitation of the multicarrier waveform structure, revealing a blockwise FFT-based implementation [3]. It basically consists of the three following stages [6], [8].

1) Estimation of the data symbols *via* a regular linear multicarrier receiver:

$$\tilde{c}_{k',m'} \triangleq \frac{1}{\sqrt{K}} \sum_{p=-\infty}^{+\infty} r[p]\breve{g}^*[p - m'L]e^{-j2\pi\frac{k'}{K}(p-m'L)} \tag{6a}$$

with $\breve{g}$ the *receive* pulse-shape verifying the perfect reconstruction condition [7].

2) Channel estimation *via* data symbol removal:

$$\bar{c}_{k',m'} \triangleq \frac{\tilde{c}_{k',m'}}{c_{k',m'}} \underset{\text{(a)}}{=} \tilde{c}_{k',m'}c^*_{k',m'}. \tag{6b}$$

Note (a): the identity is obtained by considering PSK modulations, as assumed in the rest of this paper.

3) Range-Doppler map computation *via* an IDFT/DFT pair:

$$\chi_{\text{SB}}[l,n] \triangleq \frac{1}{\sqrt{KM}} \sum_{m'=0}^{M-1} \sum_{k'=0}^{K-1} \bar{c}_{k',m'}e^{j2\pi\frac{k'}{K}l}e^{-j2\pi\frac{m'}{M}n}. \tag{6c}$$

D. Range-Doppler maps tainted with random sidelobes

As proved in [3], range-Doppler maps resulting from the MF (5) and SB (6) receivers in a clutter-free scenario can be expressed as (7) and (8), respectively. w'_{MF} and w'_{SB} denote the output thermal noise signals and

$$A^{(g,g)}(l,f) \triangleq \frac{1}{K} \sum_{p=0}^{L-1} g[p]g^*[p - l]e^{j2\pi fp} \tag{9}$$

$$A^{(g,\breve{g})}(l,f) \triangleq \frac{1}{K} \sum_{p=0}^{L-1} g[p]\breve{g}^*[p - l]e^{j2\pi fp} \tag{10}$$

are the pulse-ambiguity functions. These range-Doppler maps are especially tainted with so-called *random sidelobes* (or

$$\chi_{\mathrm{MF}}[l,n] \underset{M\gg 1}{\simeq} \alpha e^{j2\pi\left(\frac{F_d}{B}-\frac{n}{ML}\right)l_0} \sum_{k,m}\sum_{k',m'} c_{k,m} c_{k',m'}^{*} \Psi_{k',m,m',l,n} A^{(g,g)}\left(l-l_0+(m'-m)L, \frac{F_d}{B}-\frac{n}{ML}+\frac{k-k'}{K}\right) + w'_{\mathrm{MF}}[l,n] \quad (7)$$

$$\chi_{\mathrm{SB}}[l,n] \underset{M\gg 1}{\simeq} \alpha e^{j2\pi\frac{F_d}{B}l_0} \sum_{k,m}\sum_{k',m'} \frac{c_{k,m}}{c_{k',m'}} e^{j2\pi\frac{n}{M}(m-m')} \Psi_{k',m,m',l,n} A^{(g,\check{g})}\left(-l_0+(m'-m)L, \frac{F_d}{B}+\frac{k-k'}{K}\right) + w'_{\mathrm{SB}}[l,n] \quad (8)$$

$$\text{with} \qquad \Psi_{k',m,m',l,n} = e^{j2\pi\frac{k'}{K}(l-l_0+(m'-m)L)} e^{j2\pi\left(\frac{F_d}{B}L-\frac{n}{M}\right)m}/\sqrt{KM}$$

---

pedestal). This interference can actually be inferred from (7)–(8) by considering any observation cell distinct from the target's (*i.e.*, $[l,n] \neq [l_0, F_d ML/B]$). Aside from the thermal noise contribution, the double sum involves the transmitted random data symbols $c_{k,m}$ along with the pulse-ambiguity functions (9)–(10) evaluated at coordinates where they may have non-zero values. As a hint, their cuts are displayed in Fig. 2 for the two pairs of perfect reconstruction pulse-shapes that will be of interest in the rest of this paper, namely:

- the rectangular, or cyclic prefix (CP) pulses, leading to the conventional CP-OFDM waveform:

$$g_{\mathrm{CP}}[p] = \begin{cases} \sqrt{K/L} & \text{if } p \in \mathcal{I}_L \\ 0 & \text{otherwise} \end{cases}$$

$$\check{g}_{\mathrm{CP}}[p] = \begin{cases} \sqrt{L/K} & \text{if } p \in \mathcal{I}_L \setminus \mathcal{I}_{L-K} \\ 0 & \text{otherwise} \end{cases}$$

where $L-K$ defines the cyclic prefix length.
- the time-frequency localized (TFL) pulses:

$$g_{\mathrm{TFL}}[p] = \check{g}_{\mathrm{TFL}}[p] = \begin{cases} \cos\theta[p] & \text{if } p \in \mathcal{I}_{L-K} \\ 1 & \text{if } p \in \mathcal{I}_K \setminus \mathcal{I}_{L-K} \\ \sin\theta[p] & \text{if } p \in \mathcal{I}_L \setminus \mathcal{I}_K \\ 0 & \text{otherwise} \end{cases}$$

where $\{\theta[p]\}_{p=0}^{L-K-1}$ is given in [10] through numerical optimization.

Particularly, in the remainder of this paper, the influence of these pulse-shapes on the level of random sidelobes is examined.

III. THEORETICAL SINR PERFORMANCE

The impact of pulse-shaping is first assessed on the signal-to-interference-plus-noise-ratio (SINR) metrics in a clutter-free single-target scenario. This constitutes an indication regarding detection performance. Without loss of generality, we also assume in this Section that the target's Doppler frequency verifies
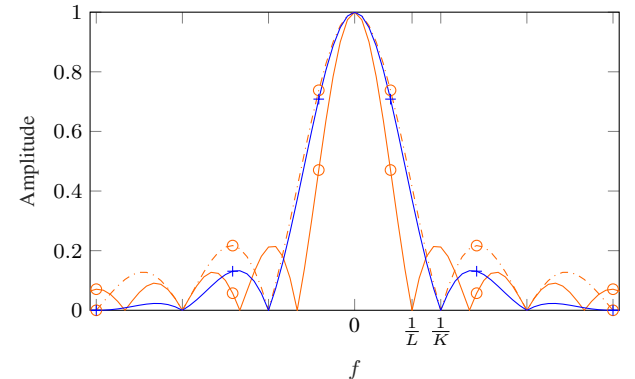
$$\frac{F_d}{B}L \triangleq \frac{n_0}{M} \quad \text{with} \quad n_0 \in \mathcal{I}_M.$$

Considering a range-Doppler map χ, we define the output SINR as

$$\mathrm{SINR}_\chi[l,n] \triangleq \frac{P_t^{(\chi)}[l_0,n_0]}{P_i^{(\chi)}[l,n]+P_{w'}^{(\chi)}}, \quad [l,n] \neq [l_0,n_0] \quad (11)$$
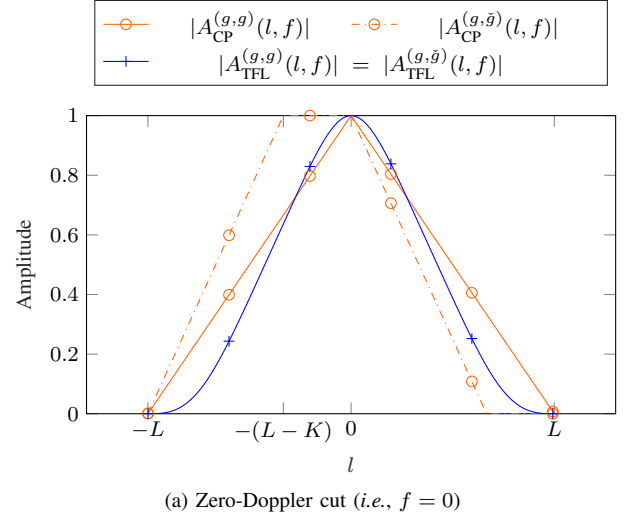
(a) Zero-Doppler cut (*i.e.*, $f = 0$)

(b) Zero-range cut (*i.e.*, $l = 0$)

Fig. 2. Pulse-ambiguity functions cuts for CP and TFL pulses ($L/K = 12/8$)

where $P_t^{(\chi)}[l_0,n_0]$, $P_i^{(\chi)}[l,n]$ and $P_{w'}^{(\chi)}$ denote the target peak, target's random sidelobes and output noise powers, respectively.

In our case, the SINR expressions of the MF and SB receivers were shown to result in (12)–(13) [3]. It is worth noting that unlike the MF, in a given scenario, the SB receiver has a uniform SINR in the range-Doppler map. In any case, both SINRs depend on the target parameters $[l_0,n_0]$ and, naturally, on the pulse-shapes *via* their pulse-ambiguity functions. As such, we represent in Figs. 3–5 different cuts of these SINRs, considering varying target positions in the range-Doppler map, for both CP and TFL pulses. We chose $K = 1024$, $L/K = 9/8$ and $M = 128$ with $\mathbb{E}\{|\alpha|^2\} = \sigma^2 = 1$.

$$\text{SINR}_{\chi_{\text{MF}}}[l,n] \underset{M \gg 1}{\widetilde{\simeq}} \frac{KM}{\sum_{k \neq 0} \left| A^{(g,g)} \left(l - l_0, \frac{n_0 - n}{LM} + \frac{k}{K} \right) \right|^2 + \sum_k \left| A^{(g,g)} \left(l - l_0 - \text{sgn}(l - l_0)L, \frac{n_0 - n}{LM} + \frac{k}{K} \right) \right|^2 + \frac{\sigma^2}{\mathbb{E}\{|\alpha|^2\}}} \tag{12}$$

$$\text{SINR}_{\chi_{\text{SB}}}[l,n] \underset{M \gg 1}{\widetilde{\simeq}} \frac{KM \left| A^{(g,\breve{g})} \left(-l_0, \frac{n_0}{LM} \right) \right|^2}{\sum_{k \neq 0} \left| A^{(g,\breve{g})} \left(-l_0, \frac{n_0}{LM} + \frac{k}{K} \right) \right|^2 + \sum_k \left| A^{(g,\breve{g})} \left(-l_0 + L, \frac{n_0}{LM} + \frac{k}{K} \right) \right|^2 + \frac{\|\breve{g}\|^2}{K} \frac{\sigma^2}{\mathbb{E}\{|\alpha|^2\}}} \tag{13}$$
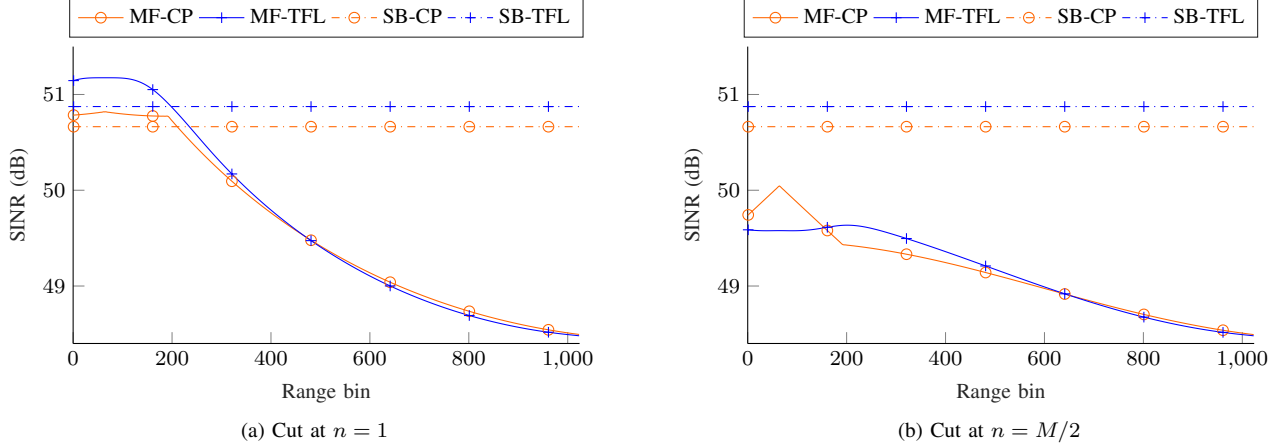

(a) Cut at $n = 1$ (b) Cut at $n = M/2$

Fig. 3. SINR Doppler cuts for target at $[l_0, n_0] = [(L-K)/2, 0] = [64, 0]$ (*i.e.*, static target, prior to the CP)
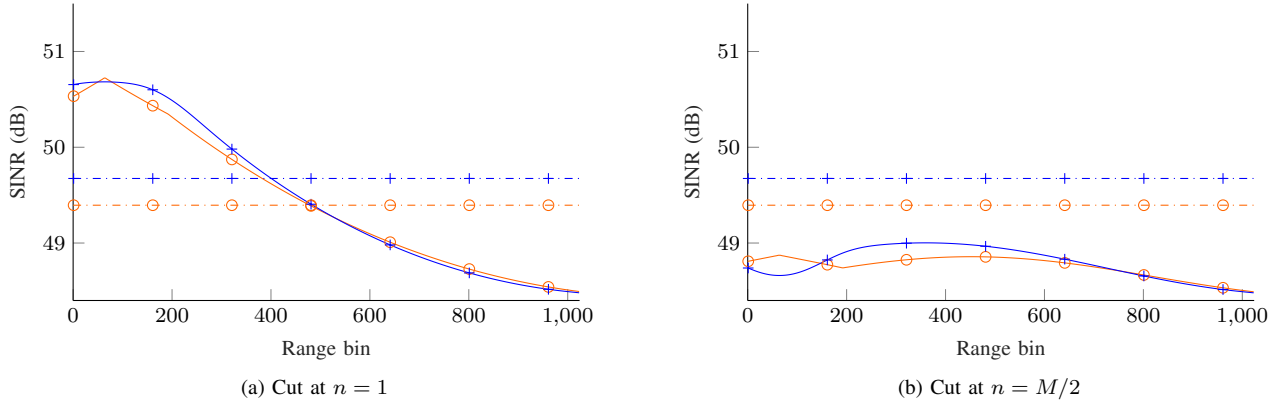

(a) Cut at $n = 1$ (b) Cut at $n = M/2$

Fig. 4. SINR Doppler cuts for target at $[l_0, n_0] = [(L-K)/2, M/4] = [64, 32]$ (*i.e.*, moving target, prior to the CP)

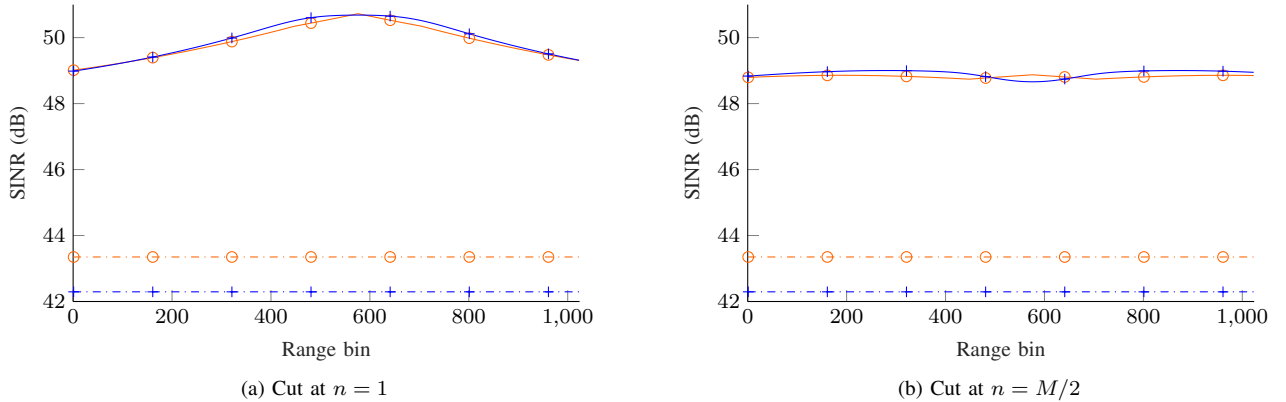(a) Cut at $n = 1$ (b) Cut at $n = M/2$

Fig. 5. SINR Doppler cuts for target at $[l_0, n_0] = [L/2, M/4] = [576, 32]$ (*i.e.*, moving target, exceeding the CP)

As expected from (12)–(13) and from the pulse-ambiguity cuts (see the solid lines in Fig. 2), we observe in these figures that the SINR of the MF decreases as the distance between the observation bin and that of the target grows. As a result, although it is always locally higher near the target, it often gets outperformed by the uniform SINR of the SB receiver farther in the map, as evidenced by Figs. 3 and 4. An exception occurs when the target's range or/and velocity becomes significant as seen in Fig. 5. Indeed, in such a case, the target peak's integration loss $\left| A^{(g,\tilde{g})}\left(-l_0, n_0/LM\right)\right|^2$ incurred by the SB (13) highly penalizes the SINR (see the blue solid and orange dashdotted lines in Fig. 2).

With the SB receiver, we can notice from Figs. 3 and 4 that a higher SINR is achieved by the TFL pulses, as compared to the CP pulses, when the target has a low range and/or high velocity, thereby confirming the observations of [9]. In these situations, CP pulses indeed suffer from their increased noise power by factor L/K and from a more significant pedestal (see the higher sidelobes of the orange dashdotted line as compared to the blue one in Fig. 2b). This gets compensated for a sufficiently distant target l_0 as seen in Fig. 5. Finally, for the MF receiver, we observe only slight improvements brought by the TFL in these figures, in particular nearby the target location where the random sidelobes power approaches 0, unlike with the CP (see $P_i^{(\chi_{\text{MF}})}[l_0, n_0]$ in (12) together with Fig. 2). They can be more significant with higher values of L/K though, since TFL pulses then offer better time-frequency localization (not represented here for the sake of compactness).

Whereas the SINR differences discussed in this Section are not always significant, we recall that they are observed when considering the pedestal induced by one single target only. Their repercussions on detection could be more severe in a realistic scenario, as hinted hereafter.

IV. Automotive scenario

We now propose to examine the influence of pulse-shaping regarding the random sidelobes interference in a typical real-world application, namely automotive DFRC. The system parameters used for the simulation are inspired from the practical implementation proposed in [11, Table 3]. As such, the DFRC system operates in the ISM band, at $F_c = 24$ GHz, occupies a bandwidth $B = 93.1$ MHz split into $K = 1024$ subcarriers, over a duration of $M = 128$ blocks. The transmit power is $P_s = -32$ dBW. We set $L/K = 9/8$ according to the power delay profile of the communication channel (see Fig. 1) while preserving a good-enough spectral efficiency.

The vehicle equipped with the DFRC system is assumed to be on the left lane of a highway, driving straight at constant velocity $v_r = 31.5$ m/s. The transmit and receive antennas are identical uniform rectangular arrays of 8×6 elements having cosine patterns but no backlobes, disposed on the front car bumper, that is at altitude $h_r = 0.5$ m from the ground. They achieve gains $G_{\text{RX}} = G_{\text{TX}} \simeq 22$ dBi in the vehicle's direction.

The radar scene is comprised of 6 target vehicles: 4 driving in our direction, 2 in the opposite one. Their parameters (namely range, radial velocity and radar cross sections) are

TABLE I
Targets parameters

Target	Motorcycle	Car 1	Truck	Car 2	Car 3	Car 4
Range (m)	80.6	177.2	30.6	96.7	41.9	122.4
Rad. vel. (m/s)	−4	0	8	4	62.7	63.1
RCS (dBsm)	5	14	35	14	12	12

provided in Table I. It also includes some ground clutter. The latter is generated following (3) with $N_c = 360$ while assuming a Gaussian distribution of the patches, *i.e.*, $\rho_{i_c,n_c} \sim \mathcal{CN}(0, \mathbb{E}\left\{|\rho_{i_c,n_c}|^2\right\})$. Their powers $\mathbb{E}\left\{|\rho_{i_c,n_c}|^2\right\}$ are computed from the radar equation for area clutter using the constant gamma reflectivity model [12] with $\gamma = -5$ dB. Ultimately, the input white Gaussian noise w is simulated with $\sigma^2 = -118$ dBW. The range-Doppler maps resulting from the sum channel of the receive antenna array and focused on the portion of interest are depicted in Fig. 6.

Due to the cumulation of the scatterers random sidelobes, the average background levels appear at least 6 dB higher than the expected post-processing noise powers. Regardless of the pulse-shape, we remark a substantially lower excess at the output of the SB as compared to the MF. Concomitantly, the measured target peak powers remain comparable from one receiver to the other. This is in line with the observations drawn in Section III for the near and/or fast targets (Figs. 3 and 4) as found in this automotive scenario. For both receivers, we also perceive improvements when using TFL pulses as compared to CP. Unlike in Section III, this is particularly visible with the MF here. Either way, these results emphasize the relevance of pulse-shaping to preserve the dynamic range even in the context of DFRC systems.

V. Conclusion and future work

In this paper, we investigated the performance of two correlation-based radar receivers, commonly encountered in OFDM DFRC, while extending them to the more general context of pulse-shaped multicarrier waveforms. Assessment was conducted for two short pulses, namely the conventional cyclic prefix baseline and the time-frequency localized pulses. We focused our analysis on the interference level related to the symbols-induced random sidelobes. Both the derived SINR expressions and the synthesized realistic automotive scenario have exhibited the interest of TFL pulses regarding interference in highly-mobile short-range scenarios, particularly when used together with the so-called symbol-based receiver. More broadly, these results tend to show the possible benefits brought by pulse-shaping to DFRC systems. Future work may include an extension of this study to alternate pulse-shaped multicarrier waveforms.
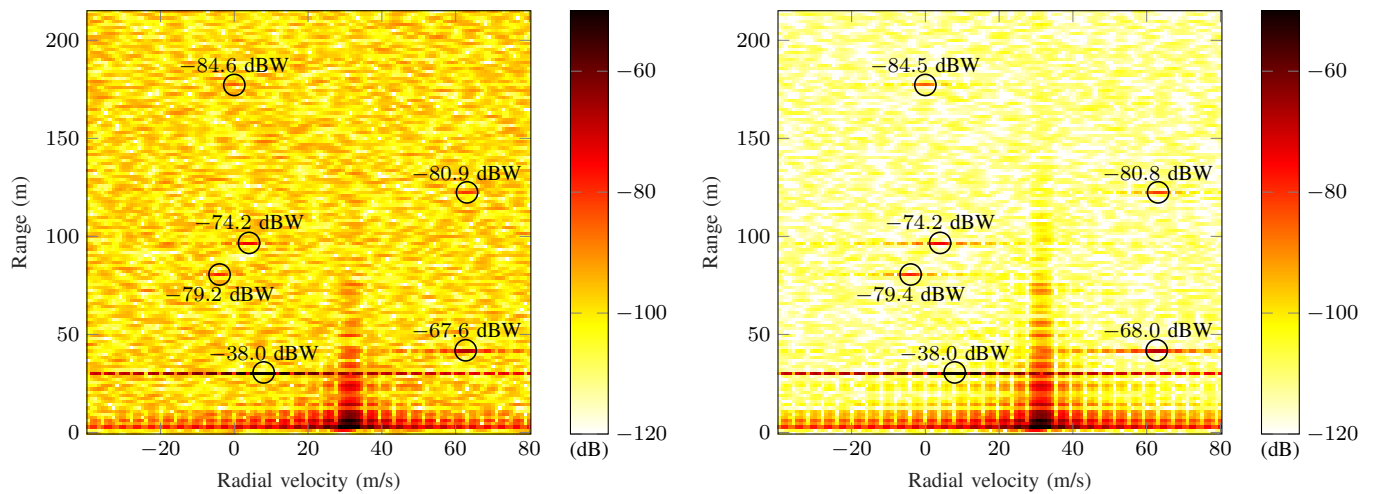
(a) Matched filter with CP pulses. Measured average background power: −97.7 dBW.

(b) Symbol-based with CP pulses. Measured average background power: −111.7 dBW.
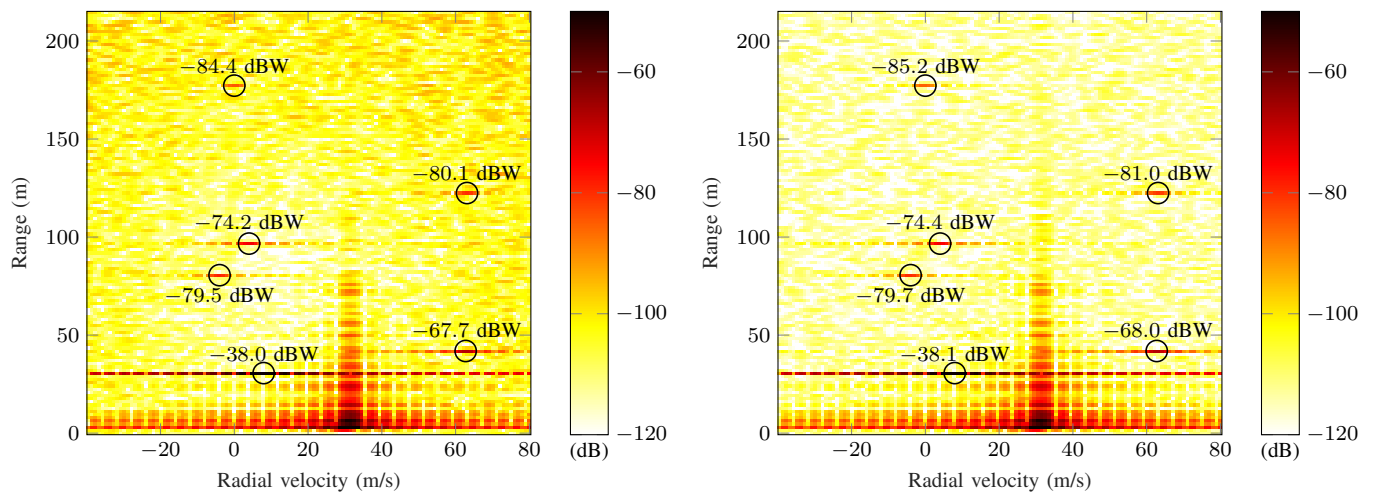
(c) Matched filter with TFL pulses. Measured average background power: −102.9 dBW.

(d) Symbol-based with TFL pulses. Measured average background power: −112.4 dBW.

Fig. 6. Range-Doppler maps of the automotive scenario focused on the portion of interest (Doppler dimension oversampled by a factor 4)

REFERENCES

[1] F. Liu, C. Masouros, A. Petropulu, H. Griffiths, and L. Hanzo, "Joint radar and communication design: Applications, state-of-the-art, and the road ahead," *IEEE Trans. Commun.*, Feb. 2020.

[2] P. Jung, "Pulse shaping, localization and the approximate eigenstructure of LTV channels," in *IEEE Wireless Commun. and Netw. Conf.*, March 2008, pp. 1114–1119.

[3] S. Mercier, S. Bidon, D. Roque, and C. Enderli, "Comparison of correlation-based OFDM radar receivers," *IEEE Trans. Aerosp. Electron. Syst.*, pp. 1–1, 2020, Early Access.

[4] A. Sahin, I. Guvenc, and H. Arslan, "A survey on multicarrier communications: prototype filters, lattice structures, and implementation aspects," *IEEE Commun. Surveys Tuts.*, vol. 16, no. 3, pp. 1312–1338, Dec. 2013.

[5] S. Koslowski, M. Braun, and F. K. Jondral, "Using filter bank multi-carrier signals for radar imaging," in *IEEE/ION Position, Location and Navigation Symp.*, May 2014, pp. 152–157.

[6] D. Roque and S. Bidon, "Using WCP-OFDM signals with time-frequency localized pulses for radar sensing," in *Proc. IEEE Asilomar Conf. Signals, Syst. Comput.*, Nov. 2016, pp. 1154–1158.

[7] D. Roque and C. Siclet, "Performances of weighted cyclic prefix OFDM with low-complexity equalization," *IEEE Commun. Lett.*, vol. 17, no. 3, pp. 439–442, March 2013.

[8] C. Sturm, T. Zwick, and W. Wiesbeck, "An OFDM system concept for joint radar and communications operations," in *Veh. Tech. Conf. Spring*, April 2009, pp. 1–5.

[9] S. Mercier, D. Roque, and S. Bidon, "Study of the target self-interference in a low-complexity OFDM-based radar receiver," *IEEE Trans. Aerosp. Electron. Syst.*, vol. 55, no. 3, pp. 1200–1212, June 2019.

[10] D. Pinchon and P. Siohan, "Closed-form expressions of optimal short PR FMT prototype filters," in *Proc. IEEE Global Telecommun. Conf.*, 2011.

[11] C. Sturm and W. Wiesbeck, "Waveform design and signal processing aspects for fusion of wireless communications and radar sensing," *Proc. IEEE*, vol. 99, no. 7, pp. 1236–1259, Jul. 2011.

[12] M. Long, *Radar Reflectivity of Land and Sea*, ser. Radar Library. Artech House, 1983.